

Enabling High Capacity and Coulombic Efficiency for Li-NCM811 Cells Using a Highly Concentrated Electrolyte

Maria A. Philip,^[a] Richard T. Haasch,^[b] Jutae Kim,^[a] Jianzhong Yang,^[c] Rachel Yang,^[a] Ivan R. Kochetkov,^[d] Linda F. Nazar,^{*[d]} and Andrew A. Gewirth^{*[a]}

Lithium metal batteries suffer from dendrite formation and the associated safety hazards of thermal runaway reactions. In this study, we report the performances of a highly concentrated electrolyte (HCE) and a dilute LiPF₆ electrolyte in lithium metal cells using LiNi_{0.8}Co_{0.1}Mn_{0.1}O₂. While the HCE exhibits lower bulk ionic conductivity than the dilute LiPF₆ electrolyte, the cell conductivity is higher for the HCE system, indicating higher thermodynamic stability of the electrolyte against the electro-

des. Full cell cycling demonstrates higher capacity for the HCE system, which declines as a function of cycle number due to the formation of decomposition products, similar to the dilute LiPF₆ system. The origin of the enhanced performance is the higher stability of the HCE against a Li metal anode as compared to the dilute LiPF₆ electrolyte. Cycling at higher temperatures further enhances the performance of the HCE, which is more thermally stable than the dilute LiPF₆ electrolyte.

1. Introduction

Lithium-ion batteries (LIBs) are approaching the theoretical limits associated with using a graphite anode and a transition-metal oxide cathode.^[1,2] As a result, lithium metal batteries (LMBs) have become the goal for post-LIB technology due to Li metal anode's high theoretical specific capacity (3860 mAh g⁻¹), low density (0.534 g cm⁻³), and low electrochemical potential (-3.040 V vs. standard hydrogen electrode).^[1,3,4] A practical LMB will require a high voltage, high capacity cathode to match the performance of the anode and will need to account for all cell components for balance of plant.^[2,5] However, the biggest factor hindering the development of LMBs is Li dendrite formation, which can cause a short circuit and eventually a fire and/or explosion, thus posing a major safety hazard.^[3,4,6,7]

There are several strategies to mitigate the hazards posed by using a lithium metal anode. The electrode-electrolyte

interface can be modified by using electrode coatings or artificial solid-electrolyte interphase (SEI) layers,^[8–10] increasing cell pressure,^[11–14] and modifying electrolytes, such as solid electrolytes and super-concentrated (often referred to as 'solvent-in-salt' or 'sparingly solvating') electrolytes.^[8,15–20] In the latter category, highly concentrated electrolytes (HCEs) are considered a safer alternative to the commercial dilute electrolytes because of the high coordination environment between the salt and solvent molecules.^[16,21] Furthermore, HCEs may be advantageous over solid and gel electrolytes due to their better interfacial/electrode wetting properties and ease of preparation.^[22]

Due to their high viscosity, HCEs often require additives, such as hydrofluoroethers (HFEs), which reduce the viscosity of the HCE and improve its ionic conductivity while maintaining thermodynamic stability.^[23,24] We recently reported the use of a HFE-modified HCE as an interlayer between solid electrolytes and lithium metal anodes to improve cell resistance and cycle life.^[25] A similar system was employed for Li–S batteries to improve cycling performance.^[26]

Recently, several groups have reported the use of HCEs with transition-metal oxide cathodes.^[21,27–30] These include a study on ether-based HCEs where stable cell cycling was demonstrated using Li anodes, and LiNi_{0.8}Co_{0.15}Al_{0.05}O₂ (NCA), LiCoO₂ (LCO), LiNi_{1/3}Co_{1/3}Mn_{1/3}O₂ (NCM333), and Li-Ni_{0.8}Co_{0.1}Mn_{0.1}O₂ (NCM811) cathodes at a rate of C/3 charge and 1 C discharge.^[27] Another study used HFE-modified sulfone-based-HCEs in cells with Li anode and NCM333 and LiNi_{0.5}Mn_{1.5}O₄ (LNMO) cathodes and demonstrated high capacity and high Li Coulombic efficiency (CE) of 99.8% in cells using NCM333 cathode.^[28] The HFE 1,1,2,2-tetrafluoroethyl-2,2,3,3-tetrafluoropropyl ether (TTE) was used to decrease the viscosity and improve the wettability of the sulfone HCEs towards the electrodes and separators.

In this paper, we use a TTE-modified HCE consisting of lithium bis(trifluoromethane sulfonyl)imide (LiTFSI) in 1,3-

[a] M. A. Philip, Dr. J. Kim, R. Yang, Prof. A. A. Gewirth

Department of Chemistry

University of Illinois at Urbana-Champaign

600 S Mathews Ave

Urbana, IL 61801, United States

E-mail: agewirth@illinois.edu

[b] Dr. R. T. Haasch

Frederick Seitz Materials Research Laboratory

University of Illinois at Urbana-Champaign

104S Goodwin Ave

Urbana, IL 61801, United States

[c] Dr. J. Yang

Argonne National Laboratory

9700 S. Cass Ave

Lemont, IL 60439, United States

[d] I. R. Kochetkov, Prof. L. F. Nazar

Department of Chemistry

University of Waterloo

200 University Ave W

Waterloo, ON N2L 3G1, Canada

E-mail: lfnaazar@uwaterloo.ca



Supporting information for this article is available on the WWW under <https://doi.org/10.1002/batt.202000192>

dioxolane (DOL) and 1,2-dimethoxyethane (DME) in full cells consisting of Li metal anode and NCM811 cathode to understand in detail the origin of the increased cyclability attendant a common cathode. We chose NCM811 because it is an advanced intercalation cathode material with a high theoretical capacity (200 mAh g^{-1}). We conducted electrochemical analysis and materials characterization to understand whether the high viscosity attendant the HCE limits its performance in a full cell and to analyze the differences between the HCE and a traditional dilute LiPF₆-based electrolyte with regard to performance in a full cell containing Li metal anode and NCM811 cathode.

2. Results and Discussion

Figure 1 shows thermogravimetric analysis (TGA) and conductivity plots for both the dilute (1 M LiPF₆ in 1:1 (v/v) ethylene carbonate (EC): ethyl methyl carbonate (EMC) electrolyte and the HCE (5.5 M LiTFSI in 5:5:2 (v/v) DOL:DME:TTE) electrolyte. TGA plots (Figure 1a, b) indicate that the HCE has higher thermal stability relative to the dilute LiPF₆ electrolyte, likely due to the higher coordination between salt and solvent molecules, which requires higher thermal energy to break.^[31–33] Another likely explanation for the higher thermal stability of the HCE is the higher inherent thermal stability of the LiTFSI salt as compared to LiPF₆.^[33–35] The dilute LiPF₆ electrolyte is volatilized at ca. 60 °C and further decomposes at ca. 130–150 °C when the remaining solvent molecules are evaporated and LiPF₆ is converted to PF₅(g) and LiF(s), as has been

previously reported.^[33] We attribute the thermal degradation of the HCE at ca. 100–150 °C to the volatilization of free solvent molecules and the decomposition at ca. 400 °C to the degradation of the remaining LiTFSI salt and coordinated solvent molecules.^[36] Indeed, the decomposition peak at ca. 400 °C aligns well with the decomposition of the LiTFSI salt shown in Figure S1. Based on Figure 1a, b and Figure S1, the order of thermal stability is: solvents < dilute solution < concentrated solution < salt, which is suggested in previous studies.^[37,38]

Figure 1c, d shows the Arrhenius bulk ionic conductivity plots for dilute LiPF₆ electrolyte and HCE, respectively. The HCE exhibits a higher activation energy barrier ($E_a = 0.190 \pm 0.020 \text{ eV}$) relative to the dilute LiPF₆ electrolyte ($E_a = 0.069 \pm 0.008 \text{ eV}$) and lower ionic conductivities in the temperature range between –15 to 53 °C. This lower ionic conductivity of the HCE correlates with its higher viscosity, measured to be $83.15 \text{ cP} \pm 0.2\%$, consistent with a prior report.^[39] Dilute (i.e., 1 M) LiPF₆ electrolytes in binary carbonate-based solvents exhibit viscosities < 5 cP.^[40–42] The Stokes-Einstein equation establishes an inverse correlation between viscosity and mobility. An electrolyte with higher viscosity, such as a HCE, will thus exhibit lower ion mobility and diffusivity. While other factors can play a role,^[43,44] in general, the lower ion mobility is associated with lower ionic conductivity for a given Li⁺ concentration. For example, this correlation was invoked in work evaluating the relationship between viscosity and conductivity for dicyanamide ionic liquids, where the authors demonstrated that higher viscosity leads to lower conductivity as a result of lower diffusion (i.e., mobility).^[45]

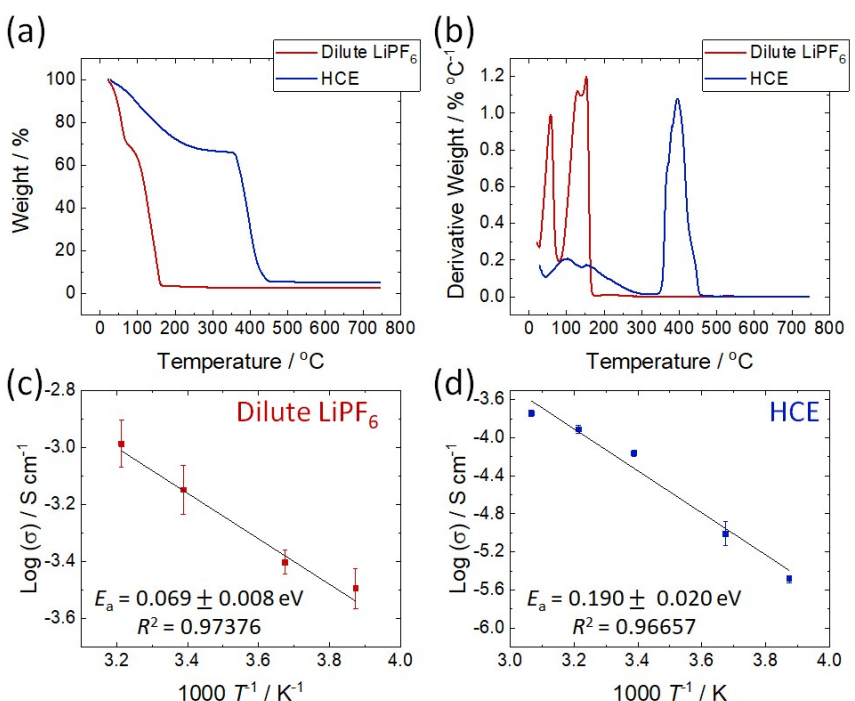


Figure 1. Characterization of electrolytes. (a, b) TGA plots for the HCE and dilute LiPF₆ electrolytes. (c, d) Arrhenius bulk ionic conductivity plots for dilute LiPF₆ electrolyte and HCE, respectively.

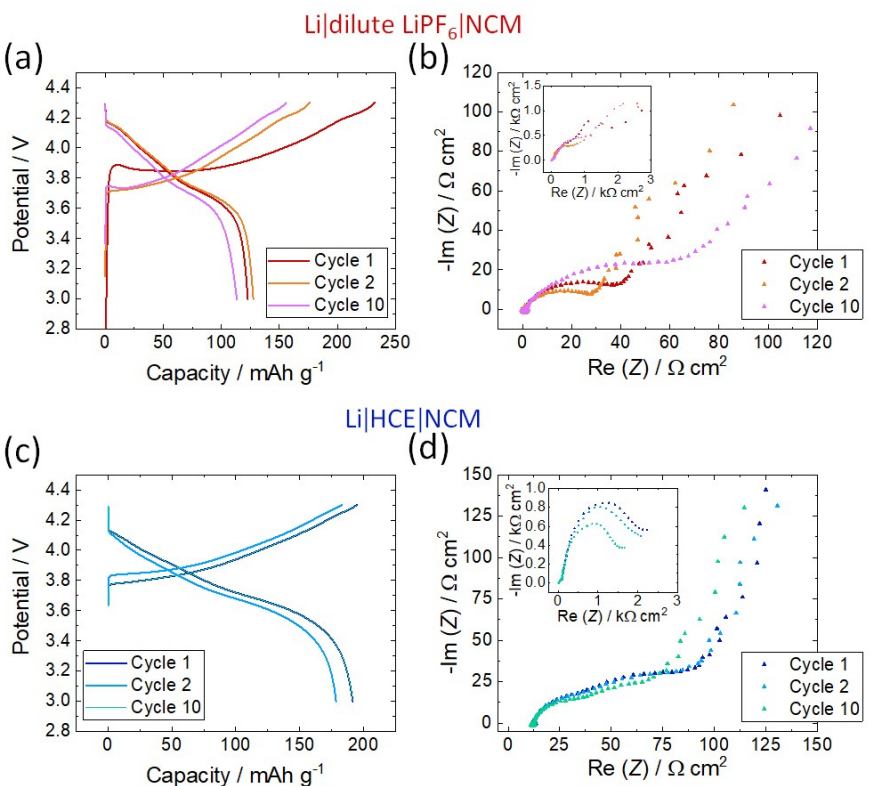


Figure 2. (a, c) Galvanostatic cycling at a rate of 1 C (200 mAh g⁻¹) and (b, d) EIS Nyquist plots for Li || NCM cells using (a, b) dilute LiPF₆ electrolyte and (c, d) HCE. We note that charge and discharge segments for cycles 1 and 10 in Figure (c) are overlapped.

Figure 2 shows sequential electrochemical impedance spectroscopy (EIS) and galvanostatic cycling results for both the HCE and dilute LiPF₆ containing cells. Figure 2a, c show charge/discharge curves for cells consisting of a Li metal anode, a NCM811 cathode, and the two different electrolyte systems. We note that the capacities observed in these two figures are artificially low due to pauses between galvanostatic cycles in order to conduct EIS measurements. We discuss the effect of the electrolytes on discharge capacities later in Figure 5 where galvanostatic cycling experiments was conducted without any pauses (*vide infra*). Figure 2a shows the charge/discharge curve obtained from the dilute LiPF₆ electrolyte system. The curve shows the presence of four plateaus, more clearly seen in the differential capacity (Figure S2a). The shape of the curve and the overall capacity is consistent with prior reports.^[46–48] We note the first charge segment in Figure 2a has a higher capacity relative to both subsequent cycles and the first discharge segment. The low CE for the first cycle is associated with the formation of the SEI and the consumption of active Li⁺, as reported previously.^[49,50]

Figure 2c shows the corresponding charge/discharge curve for the HCE system. In contrast to the dilute LiPF₆ system, the discharge capacity remains roughly constant through the first ten cycles. Thus, the HCE cell exhibits substantially greater capacity relative to the dilute LiPF₆ cell.

Figure 2b, d show the corresponding Nyquist plots obtained at the end of a full cycle with the cell in the discharged

condition. Figure S3 shows the equivalent circuit used to fit the Nyquist plots and an exemplary fit. The fit excludes the high frequency region of the inductance loop and low frequency region associated with diffusion. The equivalent circuit consists of two components in series: (1) a resistor representing bulk electrolyte resistivity (R_{bulk}) and (2) a resistor (R_{int}) parallel to a constant phase element (CPE_{int}) representing the interfacial component. The R_{int} value represents the response from both electrode|electrolyte interfaces in the cell. The results from the fit are given in Table 1.

Figure 2b shows the impedance of the dilute LiPF₆ cell. The figure shows that the impedance between cycle 2 and cycle 10 increases, specifically the interfacial resistivity which increases from 34 Ω cm² to 68 Ω cm². This impedance plot is consistent with that reported previously.^[51,52] The inset to Figure 2b shows the low frequency region of the impedance. The overall resistivity appears to increase with cycle, an effect that has

Table 1. Resistivity values for the Nyquist plots in Figure 2.

Cell	Cycle	R_{bulk} [Ω cm ²]	R_{int} [Ω cm ²]
Li dilute LiPF ₆ NCM	1	0.71	47
	2	0.70	34
	10	0.66	68
	1	12	50
Li HCE NCM	2	11	52
	10	11	43

been attributed to decomposition of the electrolyte on the surfaces of both electrodes.^[52,53]

Figure 2d shows the impedance obtained in the mid-frequency region for the HCE cell. The figure shows this impedance moderately decreases over the 10 cycles shown here and decreases from $52 \Omega \text{cm}^2$ at cycle 2 to $43 \Omega \text{cm}^2$ at cycle 10. A previous study on a cell using a LCO cathode observed a similar decrease in the mid-frequency semi-circle as a function of cycling, which the authors attributed to more facile (de)lithiation of the cathode.^[54] In another study, authors attributed the decrease in impedance seen in cells containing $\text{LiNi}_{0.6}\text{Co}_{0.2}\text{Mn}_{0.2}\text{O}_2$ (NCM622) cathodes to an increasing effective surface area of Li anodes. This increase in surface area would decrease the overall resistance of the cell.^[55] The inset in Figure 2d shows the low frequency region of the impedance. Here, the overall resistivity appears to decrease with cycle, an effect we attribute to slow permeation of HCE into cathode

particles as a result of the electrolyte's high viscosity (*vide infra*).

There are two general methods to deconvolute the anode and cathode electrode|electrolyte interface contributions to the impedance observed in Figure 2b.^[54] First, a complex equivalent circuit model may be used to account for the various contributions from both the anode and cathode.^[56–59] Second, symmetric cells and Randles-type equivalent circuits can be used to determine each electrode's contribution to the overall cell resistivity, a method we favor.^[53,54] Separated electrode contributions were obtained by conducting EIS on symmetric cells at the time of fabrication and again after 48 h. This method allows us to evaluate the temporal thermodynamic stability of electrolytes against electrodes. Figure 3 shows the temporal evolution of impedance in $\text{Li}||\text{Li}$, NCM||NCM, and $\text{Li}||\text{NCM}$ cells for both dilute LiPF_6 electrolyte and HCE. Figure 4 shows the resistivity values extracted from

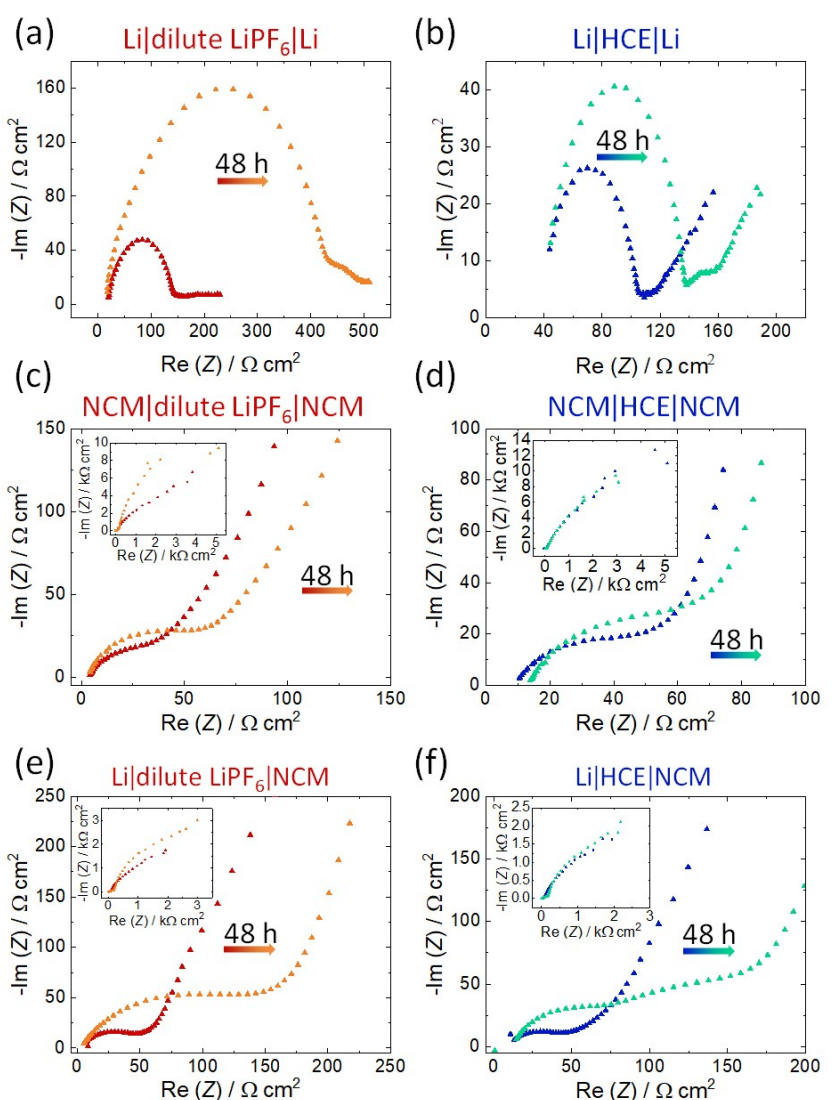


Figure 3. Temporal evolution of impedance in (a, b) $\text{Li}||\text{Li}$, (c, d) NCM||NCM, and (e, f) $\text{Li}||\text{NCM}$ cells over 48 h using (a, c, e) dilute LiPF_6 electrolyte and (b, d, f) HCE. The insets to figures (c, d, e, f) show expansions of the low-frequency region.

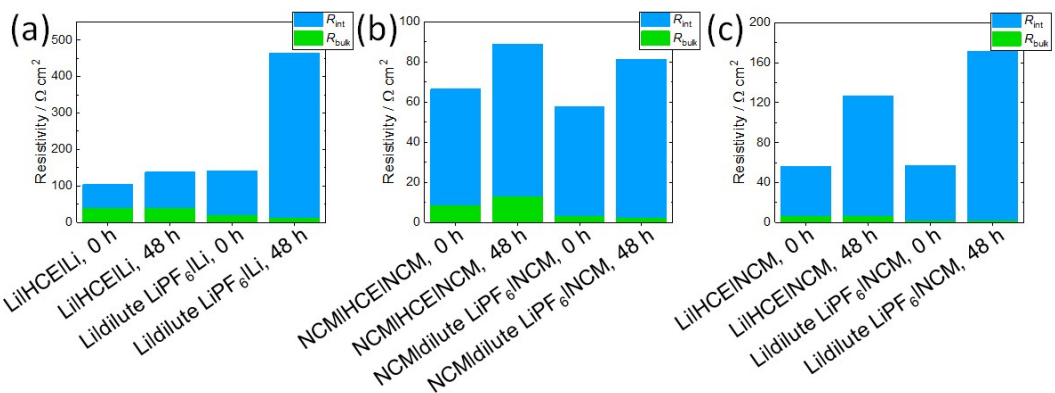


Figure 4. Interfacial (blue) and bulk (green) resistivity values extracted from the temporal evolution of impedance plots in Figure 3 for (a) $\text{Li} \parallel \text{Li}$, (b) $\text{NCM} \parallel \text{NCM}$, and (c) $\text{Li} \parallel \text{NCM}$ cells consisting of dilute LiPF_6 and HCEs. Resistivity values are provided in Table S1.

Figure 3 (provided in Table S1) using the same equivalent circuit as for Figure 2 (shown as inset in Figure S3).

Figure 3a-d and Figure 4a-b show the temporal evolution of impedance for $\text{Li} \parallel \text{Li}$ and $\text{NCM} \parallel \text{NCM}$ symmetric cells. Contributions from the Li anode and the NCM cathode in a full cell can be deconvoluted by first identifying individual contributions using symmetric cells. At both time $t = 0 \text{ h}$ and $t = 48 \text{ h}$, the $\text{Li} \parallel \text{HCE} \parallel \text{Li}$ cell (Figure 3b, 4a) exhibits overall lower resistivity than the $\text{Li} \parallel \text{dilute LiPF}_6 \parallel \text{Li}$ cell (Figure 3a, 4a), as has been demonstrated previously,^[60] indicating that the HCE is more thermodynamically stable against Li metal than the dilute LiPF_6 electrolyte within a 48 h period. The higher thermodynamic stability of HCEs is a known advantage of concentrated electrolytes relative to dilute systems.^[16,32,39] Although the HCE exhibits lower ionic conductivity than the dilute LiPF_6 electrolyte (Figure 1c, d), that bulk ionic conductivity is dominated by the higher interfacial resistivity in both cells as can be seen in Figure 4a and Table S1, resulting in the $\text{Li} \parallel \text{HCE} \parallel \text{Li}$ cell having an overall lower resistivity than the $\text{Li} \parallel \text{dilute LiPF}_6 \parallel \text{Li}$ cell. We note that the bulk resistivity of the electrolytes is lower in the $\text{NCM} \parallel \text{NCM}$ cells as compared to the $\text{Li} \parallel \text{Li}$ cells; this artifact is likely due to the fact that the effective surface area of the NCM electrode is larger than its geometric area due to its high porosity, leading to a lower bulk resistivity.

The $\text{NCM} \parallel \text{HCE} \parallel \text{NCM}$ cell (Figure 3d, 4b) exhibits higher resistivities than the $\text{NCM} \parallel \text{dilute LiPF}_6 \parallel \text{NCM}$ cell (Figure 3c, 4b) at time of cell fabrication ($t = 0 \text{ h}$) and 48 h later. We attribute this higher resistivity of the HCE cell to the slower permeation of the electrolyte into the NCM electrodes as a result of the HCE's higher viscosity (*vide infra*). This slower permeation is expected owing to our use of cathodes which have been neither pressed nor calendared. Additionally, the evolving NCM interface may contribute to this higher resistivity.

While both $\text{Li} \parallel \text{HCE} \parallel \text{NCM}$ (Figure 3f, 4c) and $\text{Li} \parallel \text{dilute LiPF}_6 \parallel \text{NCM}$ (Figure 3e, 4c) cells exhibit similar resistivities at $t = 0 \text{ h}$, the resistivity of the HCE cell is lower than that of the dilute LiPF_6 cell at $t = 48 \text{ h}$. Therefore, we conclude that the increase in cell resistivity for the dilute LiPF_6 cell relative to that of the

HCE cell is primarily due to the higher thermodynamic instability of this electrolyte against the Li anode.

Figure 5 shows discharge capacities and CEs obtained from the $\text{Li} \parallel \text{HCE} \parallel \text{NCM}$ and $\text{Li} \parallel \text{dilute LiPF}_6 \parallel \text{NCM}$ cells over 200 cycles. The HCE cell maintains higher discharge capacity and CE relative to the dilute LiPF_6 cell throughout the 200 cycles studied here. Over multiple trials, the average capacity at cycle 20 of the HCE cell was $219 \pm 2 \text{ mAh g}^{-1}$ while that of the dilute LiPF_6 cell was $164 \pm 7 \text{ mAh g}^{-1}$. The better performance of the HCE cell can be attributed, at least in part, to the higher thermodynamic stability of the electrolyte against Li metal anode as compared to the dilute LiPF_6 electrolyte as demonstrated in Figure 4a. Furthermore, although the first cycle in both cells shows lower CE, as has been reported previously,^[61] the subsequent cycles in the HCE cell exhibit an average CE of 100.2% as compared to the dilute LiPF_6 cell with an average CE of 93.4%. Prior studies have reported CEs greater than 99% for

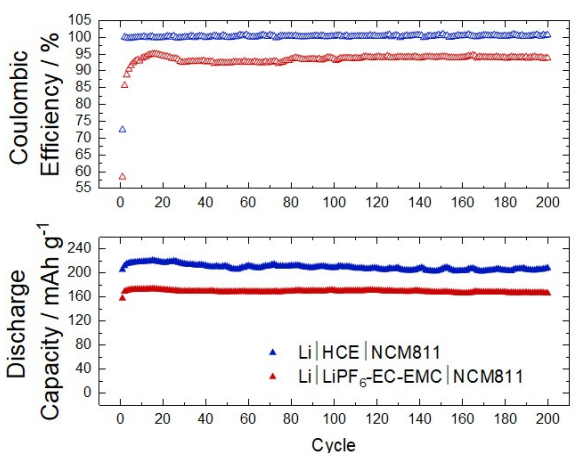


Figure 5. Discharge capacities and CEs over 200 cycles for $\text{Li} \parallel \text{NCM}$ cells at room temperature (22°C) with both HCE and dilute LiPF_6 electrolytes (ca. 2 mg cm^{-2} loading of NCM). Cells were cycled at a rate of 1C (200 mAh g^{-1}).

HCE systems in Li metal cells,^[27,28,62] but no reports have reported a CE that exceeds 100%.

The greater than theoretical discharge capacity and CE > 100% may be a consequence of a capacitive contribution to intercalation. Figure S6a shows an exemplary cyclic voltammogram (CV) of a Li|HCE|NCM cell. Using Dunn's method where current is plotted versus scan rate on logarithmic scales for the positive and negative sweeps (Figure S6b, c), we can obtain slopes from the linear plots, where a value of 0.5 indicates a diffusion-controlled, Faradaic intercalation process, and a value of 1 indicates a capacitance-dominated process.^[63] We calculated the slope to be 0.59 ± 0.01 for the positive (charge) sweep and 0.70 ± 0.01 for the negative (discharge) sweep. These slope values indicate that the Li|HCE|NCM cells undergo primarily Faradaic intercalation processes with more pseudocapacitance for discharge than charge. This hysteresis between pseudocapacitance for discharge and charge accounts for the higher capacitance observed for discharge over charge and the > 100% CE. The use of ball milling during cathode preparation may result in smaller particles exhibiting this modest pseudocapacitance. We note that while the dilute LiPF₆ cell might include a pseudocapacitance process, the HCE's higher concentration will contribute to higher pseudocapacitance.

Figures S4 and S5 show cycling data at room temperature and 40 °C, respectively, for cells constructed with higher loadings of cathode active material ($\sim 5 \text{ mg cm}^{-2}$). The cell cycled using dilute LiPF₆ electrolyte exhibits an average CE of 98.4% at room temperature (Figure S4). The Li|HCE|NCM cell cycled at 40 °C (Figure S5) exhibits higher discharge capacity than the cell cycled at room temperature (Figure S4). We attribute this higher capacity seen at an elevated temperature to the slow permeation of the HCE into the cathode particles at the lower temperature as a result of its high viscosity. Because of increased permeation at elevated temperatures, there is better cathode wetting and therefore higher capacity.

Figure 6a, b shows the discharge capacities for cells fabricated with lower loadings of NCM active material using both the dilute LiPF₆ and the HCEs at various C-rates. At a rate of 1 C, the Li|HCE|NCM cell exhibits discharge capacities ca. 220 mAh g⁻¹ at room temperature and at 40 °C. Compared to the high loading cells in Figure S4 and S5, the data indicate

that elevated temperatures are necessary for full permeation of the viscous HCE into the cathode with higher loadings of active material. Cycling cells constructed with lower loadings of active cathode material at elevated temperatures does not impart higher discharge capacities as demonstrated in Figure 6a, b by the Li|HCE|NCM cell cycled at 22 °C and 40 °C. Cycling allows the HCE to fully wet the cathode, as demonstrated by the decreasing resistivity as a function of cycling of the Li|HCE|NCM cell in Figure 2d.

At all C-rates studied in Figure 6a, b (1–3 C), the HCE cell exhibits higher discharge capacities than the dilute LiPF₆ cell. We attribute this enhanced performance of the HCE cell to its higher thermodynamic stability against Li metal, particularly since cells were allowed to rest 24 to 48 h prior to cycling. However, when cycling at rates faster than 1 C, the HCE cell exhibits a larger drop in discharge capacity relative to that of the dilute LiPF₆ cell. This drop in discharge capacity observed in the HCE system for higher C-rates is observed at both 22 °C (i.e., room temperature) and 40 °C. We speculate this larger drop in capacity to be a result of the HCE's higher viscosity and lower mobility, although kinetic limitations of Li⁺ transfer across the Li|HCE|NCM interfaces induced at elevated temperatures may be a factor. Furthermore, both the dilute LiPF₆ and HCE cells exhibit higher discharge capacities at 40 °C than at 22 °C. Similar to the HCE cell at 22 °C, the HCE cell at 40 °C exhibits a larger drop in capacity at higher C-rates relative to the dilute LiPF₆ cell, likely due to its higher viscosity.

Figure 7 shows scanning electron microscopy (SEM) images of a pristine Li anode and Li anodes extracted from the Li|NCM cells following 200 galvanostatic charge/discharge cycles. The SEM images of the surface of pristine Li metal (Figure 7a, b) show evidence of non-uniformity as evidenced by high-contrast features, which is common for commercial Li metal.^[64]

SEM images of the surface of a Li anode from a Li|dilute LiPF₆|NCM cell (Figure 7c, d) show mossy features. A prior study demonstrated mossy Li growth in a Li|Cu cell with LiPF₆-EC-diethyl carbonate (DEC) electrolyte arising as a result of nonuniform nucleation.^[65] Conversely, the low-magnification SEM image of the surface of a Li anode from Li|HCE|NCM cell (Figure 7e) shows no apparent features. The high-magnification image (Figure 7f) shows electron-rich (i.e., bright) regions

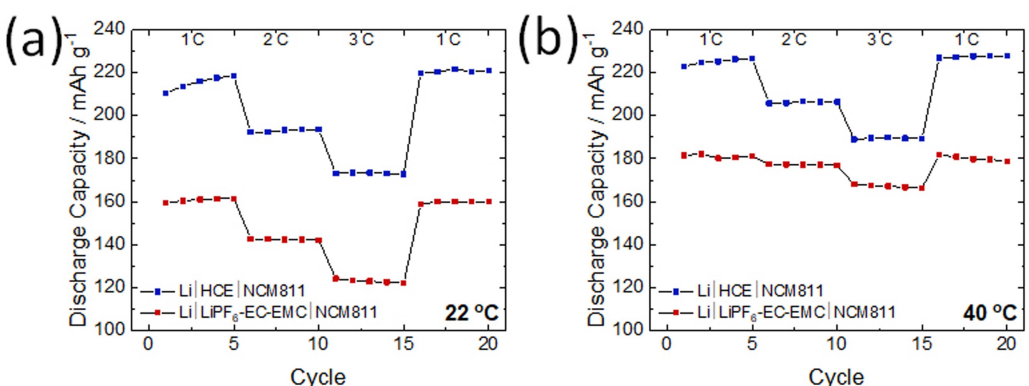


Figure 6. C-rate studies for Li|HCE|NCM and Li|dilute LiPF₆|NCM. Discharge capacities at different C-rates at (a) 22 °C and (b) 40 °C.

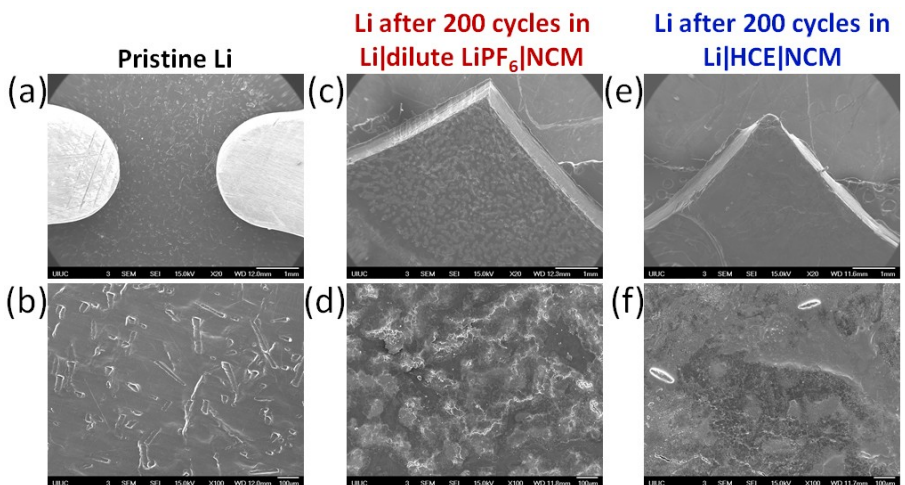


Figure 7. SEM images of (a, b) pristine Li, (c, d) Li anode after 200 cycles in a Li|dilute LiPF₆|NCM cell, and (e, f) Li anode after 200 cycles in a Li|HCE|NCM cell. In Figure 7a, the bright, electron-rich regions on the left and right are SEM sample spring clip holders. The scale bar is 1 mm for the figures in the top row and 100 μ m for the figures in the bottom row.

similar to those seen on the pristine Li metal (Figure 7b), indicating the retention of some of the original Li metal features. Additionally, the Li anode from the HCE cell exhibits darker, electron-poor features, which are larger and more compact than the features seen in the dilute LiPF₆ cell, indicating more uniform Li deposition.

We attribute this more uniform deposition on the surface of Li metal anode in a cell with a HCE to the higher local pressure of the more viscous electrolyte exerted against the anode, as has been suggested in a previous study.^[18] Furthermore, prior studies have demonstrated that the higher surface roughness on Li anodes cycled with dilute electrolytes indicates that the electrolyte degrades against Li metal resulting from poor thermodynamic stability and/or Li dendrites or “dead Li” formed on the surface of the anode, effects that are suppressed using a HCE.^[18,28,66]

During the deconstruction of cycled cells to prepare samples for SEM imaging, we observed a thin black layer on the surface of the Li anode from the dilute LiPF₆ cell, whereas the surface of the Li anode from the HCE cell was shiny, similar to the surface of pristine Li. The darkening of the surface of Li metal in dilute LiPF₆ electrolytes is consistent with prior reports suggesting the presence of dendritic Li deposition and/or chemical reaction of the electrolyte with Li metal to form an SEI.^[67,68]

Figure 8 shows normalized X-ray photoelectron spectroscopy (XPS) spectra obtained from Li anodes extracted from Li|dilute LiPF₆|NCM cells at different cycles, and Table S2 gives the corresponding peak positions and assignments. Figure S7 shows the XPS spectra obtained from pristine Li metal for reference, and Figure S8 shows the XPS survey scans of Li anodes. The pristine Li anode (Figure S7) shows the presence of

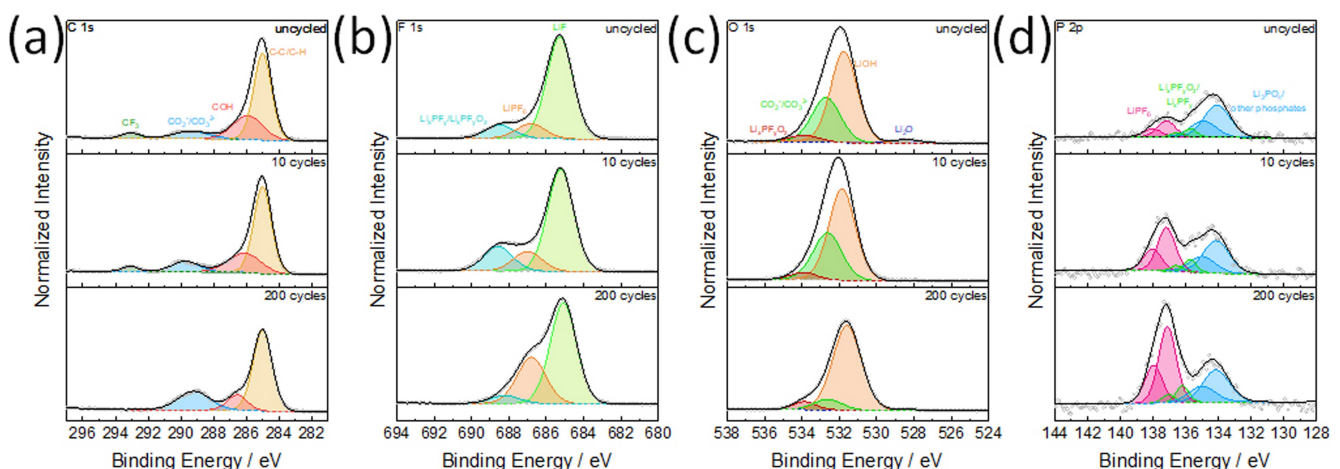


Figure 8. Normalized XPS spectra of Li anodes from Li|dilute LiPF₆|NCM cells at different cycles: 0 (top), 10 (middle), and 200 (bottom). (a) C 1s, (b) F 1s, (c) O 1s, and (d) P 2p regions. Spectra for each elemental region at 10 and 200 cycles were normalized to the largest peak in the spectrum of the Li anode from the uncycled cell.

surface degradation products, namely carbon and oxygen species, due to the fact that Li anodes were briefly exposed to the environment prior to transferring them to the XPS chamber.

All spectra in Figure 8 show the same type of degradation products before and after 200 cycles, indicating that degradation occurs prior to cycling as demonstrated in Figures 3 and 4. The degradation products are COH, carbonates, CF_3 , LiF, Li_xPF_y phosphates, Li_2O , and LiOH. Within each elemental region, the relative prominence of different species changes with cycle number. For example, LiF decreases relative to LiPF_6 (Figure 8b). The carbonate species (CO_2^- and CO_3^{2-}) increase with respect to other organic species (Figure 8a). The hydroxides increase relative to other oxides (Figure 8c). The phosphates increase with respect to LiPF_6 (Figure 8d). The spectra thus suggest the evolution of the distribution of degradation products as a function of cycle number. The inorganic LiF is suppressed relative to organic, solvent decomposition products and adventitious LiPF_6 . This observation is consistent with a ‘two-sublayer SEI’ model where the inner layer of the SEI is comprised primarily of inorganic species, and the outer layer is comprised of organic species.^[66,70] The Li 1s spectra (Figure S9) show that the Li signal decreases with cycle number, which suggests that the Li surface and inorganic Li species are buried by organic degradation products.

The increase in decomposition products on the surface of Li metal as a function of cycle number for the Li|dilute LiPF_6 |NCM cell suggests that a dilute LiPF_6 electrolyte is highly unstable against Li metal and will react, forming resistive products, as has been reported previously.^[71,72] The LiPF_6 decomposition mechanism involves conversion of LiPF_6 to LiF and Li_xPF_y , and subsequent oxidization or hydrolysis of the later product to form $\text{Li}_x\text{PF}_y\text{O}_z$.^[73,74] The free solvent EC and EMC molecules also degrade to form the other organic and inorganic species.^[72,75,76]

Figure 9 shows normalized XPS spectra for Li anodes extracted from Li|HCE|NCM cells at different cycles, and

Table S3 gives the corresponding peak positions and assignments. Similar to the dilute LiPF_6 system, the Li anodes from the HCE cells show the same type of degradation products both before and after 200 cycles, which include COR, carbonates, LiF, $\text{N}-\text{SO}_x$, Li_xSO_y , LiOH, and $(\text{CH}_2-\text{CH}_2-\text{O})_n$. The carbonate, CHF, and adventitious LiTFSI C–F peaks increase relative to the adventitious hydrocarbon peak as a function of cycle number (Figure 9a). Likewise, the C–F peak in the F1s spectra also increases relative to LiF, a LiTFSI decomposition product (Figure 9b). The O1s and S2p spectra (Figure 9c,d) show a decrease of oxygen- and sulfur-containing decomposition products relative to adventitious LiTFSI. These results are consistent with those of the dilute LiPF_6 system in which a ‘two-sublayer SEI’ forms with the inorganic species buried under the organic ones, which is coated with the HCE.

3. Conclusions

In this paper, we reported the performance of a LiTFSI-DOL-DME-TTE HCE in a lithium metal cell with NCM811 and compared the performance of this HCE to that of a commercial, dilute LiPF_6 electrolyte. We show that while the bulk impedance associated with the HCE is high, the overall cell resistivity is dominated by the Li|electrolyte interface, where the HCE exhibits lower resistivity than the dilute LiPF_6 electrolyte. Full cell cycling of Li||NCM with the HCE demonstrated initial high capacity above the theoretical 200 mAh g⁻¹ and CE > 100%, some of which is due to pseudocapacitance. The HCE cell’s capacity declined as a function of cycle number due to the formation of decomposition products, as demonstrated by XPS analysis. Likewise, XPS analysis shows buildup of degradation products for the cell with the dilute LiPF_6 electrolyte as a function of cycle number. EIS, galvanostatic cycling, and SEM show the origin of the enhanced performance is the higher stability of the HCE against Li metal anode as compared to the dilute LiPF_6 electrolyte. Cycling at higher temperatures further

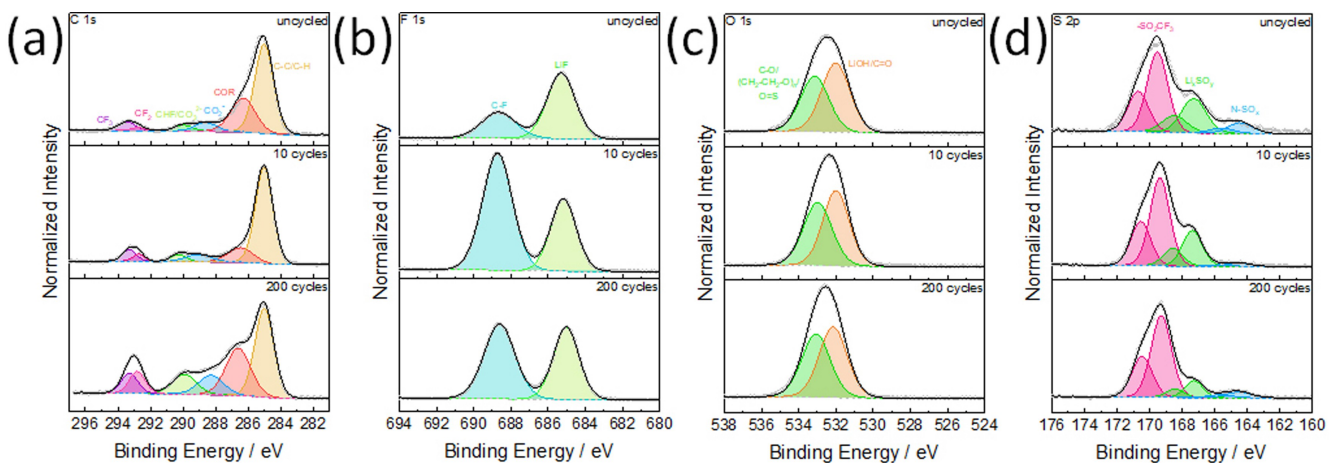


Figure 9. Normalized XPS spectra of Li anodes from Li|HCE|NCM cells at different cycles: 0 (top), 10 (middle), and 200 (bottom). (a) C1s, (b) F1s, (c) O1s, and (d) S2p regions. Spectra for each elemental region at 10 and 200 cycles were normalized to the largest peak in the spectrum of the Li anode from the uncycled cell.

enhances the performance of the HCE, which we found to be more thermally stable than the dilute LiPF₆ electrolyte.

Experimental Section

Electrolyte Preparation

All materials were handled in an Ar environment. The dilute LiPF₆ electrolyte was a 1 M solution of LiPF₆ in 1:1 (v/v) EC and EMC (battery grade, Sigma-Aldrich) and was used as-received. The HCE was prepared using LiTFSI (Sigma-Aldrich), DOL (Sigma-Aldrich), DME (Sigma-Aldrich), and TTE (Synquest Laboratories). All solvents were dried under molecular sieves, and the LiTFSI salt was dried at 130 °C under vacuum prior to use. The HCE was prepared by first dissolving LiTFSI (10.05 g) in a mixture of DOL (2.5 mL) and DME (2.5 mL), resulting in a 7.3 M concentration. This neat HCE was then diluted at 1:5 (v/v) TTE to DOL-DME for a final concentration of 5.5 M as the neat HCE (without added TTE) was too viscous for practical use.

Cathode Preparation

Cathodes were prepared from a slurry consisting of 8:1:1 (by wt) NCM811 (MSE Supplies), poly(vinylidene fluoride) (PVDF, Kynar Flex), and conductive carbon (Super P Li, Timcal) in *n*-methyl-2-pyrrolidone (NMP, Sigma-Aldrich). To prepare slurries with ca. 2 mg cm⁻² active material, the conductive carbon and active material were ball milled and then ground in a mortar and pestle to decrease particle size. This powder was then added to a solution of PVDF in NMP that was mixed using a planetary mixer (Thinky). The resulting slurry was vortexed and mixed using a planetary mixer. Afterwards, the slurry was cast on an aluminum foil current collector by using a doctor blade set at a height of 75 µm. The cathode was dried on a hot plate at 65 °C and subsequently dried again overnight in an oven at 120 °C. Electrode punches were dried on a hot plate at 100 °C before being transferred into an Ar-filled glovebox. Slurries with ca. 5 mg cm⁻² active material were prepared by first ball milling the active material on its own prior to ball milling with the conductive carbon. This slurry was cast on an aluminum foil current collector by using a doctor blade set at a height of 175 µm.

Coin Cell Assembly and Electrochemical Measurements

Electrochemical measurements were conducted using CR2032 coin cells (MTI Corporation). Full cells (Li||NCM) were prepared using 40 µL of electrolyte (HCE or dilute LiPF₆ electrolyte), a separator (25 µm thick, 16 mm diameter, Celgard 2325), Li (0.6 mm thick; 16 mm diameter, 99.9% MTI Corporation), and NCM811 (7.9 mm diameter). Symmetric cells (Li||Li and (NCM||NCM) were prepared in a similar manner. Blocking cells used to determine bulk ionic conductivity of the electrolytes were prepared using 30 µL of electrolyte and a separator sandwiched between stainless steel electrodes.

Galvanostatic cycling studies were conducted with potentials between 3.0 and 4.3 V. Measurements were carried out on an Arbin electrochemical workstation (BT2043, Arbin Instruments) and a Neware BTS4000 cycler for long-term cycling studies and on a BioLogic Science Instruments impedance analyzer (SP-150) for sequential cycling and EIS studies. All coin cells used for galvanostatic cycling were allowed to rest for at least 24 h prior to cycling to allow permeation of the electrolyte through the separator and electrodes. We calculated CE as the discharge

capacity divided by the charge capacity, as is common practice.^[30,77–79]

Galvanostatic EIS measurements were conducted by using a perturbation amplitude of 20 µA. Bulk ionic conductivity measurements in blocking cells were conducted in the frequency range of 1 MHz to 100 mHz. EIS measurements conducted as a function of time in both full and symmetric cells were carried out in the range of 10 kHz to 10 mHz. Finally, measurements in Li||NCM cells conducted alongside galvanostatic cycling were carried out at 1 MHz to 7 mHz.

CV measurements were performed using CH Instruments potentiostats. The potential of the working electrode was swept between 3.0 V and 4.3 V vs. Li/Li⁺. CV measurements were consecutively taken at scan rates varying from 0.2 mV s⁻¹ to 0.5 mV s⁻¹.

Materials Characterizations

Thermal stability studies were conducted using a Q50 TGA (TA Instruments). All samples were analyzed under nitrogen with a heating rate of 10 °C min⁻¹ from room temperature to 750 °C. Viscosity measurements were conducted using a ViscoLab 4000 viscometer (PAC-Cambridge Viscosity) at room temperature (24 °C). SEM images were collected on a JEOL, JSM-7000F (GenTech) with an accelerating voltage of 15.0 kV.

XPS measurements were conducted using a monochromatic Al Kα source on a Kratos Axis Ultra spectrophotometer (Kratos Analytical) with an analytical energy resolution of 0.4 eV. The binding energies were calibrated relative to the C1s peak at 285.0 eV. The S2p peaks were fitted with the Gaussian line shape in CasaXPS software (Casa Software Ltd.) with 1.18 eV energy splitting between the S2p_{1/2} and S2p_{3/2} peaks. Similarly, the P2p peaks were fitted with 0.84 eV splitting.

Acknowledgements

This work was partially supported as part of the Joint Center for Energy Storage Research (JCESR), an Energy Innovation Hub funded by the U.S. Department of Energy, Office of Science, Basic Energy Sciences. M. A. P. acknowledges a Bahrke Fellowship from the Department of Chemistry at the University of Illinois. L.F.N. acknowledges partial support from NSERC for financial support through their Discovery and Canada Research Chair programs. The characterization of materials was carried out in part in the Materials Research Laboratory Central Research Facilities, University of Illinois.

Conflict of Interest

The authors declare no conflict of interest.

Keywords: concentrated electrolyte • electrochemistry • interfaces • lithium metal anode • NCM811 cathode

- [1] X. B. Cheng, R. Zhang, C. Z. Zhao, Q. Zhang, *Chem. Rev.* **2017**, *117*, 10403.
- [2] C. U. Jeong, S.-Y. Lee, J. Kim, K. Y. Cho, S. Yoon, *J. Power Sources* **2018**, *398*, 193.
- [3] C. Fang, X. Wang, Y. S. Meng, *Trends in Chem.* **2019**, *1*, 152.

- [4] W. Xu, J. Wang, F. Ding, X. Chen, E. Nasybulin, Y. Zhang, J.-G. Zhang, *Energy Environ. Sci.* **2014**, *7*, 513.
- [5] A. Eftekhari, *ACS Sustainable Chem. Eng.* **2018**, *7*, 3684.
- [6] S. S. Zhang, *ACS Appl. Energy Mater.* **2018**, *1*, 910.
- [7] L. French, G. K. Sethi, J. A. Maslyn, N. P. Balsara, *Front. Energy Res.* **2019**, *7*, 115.
- [8] L. Li, S. Li, Y. Lu, *Chem. Commun.* **2018**, *54*, 6648.
- [9] G. Zheng, S. W. Lee, Z. Liang, H. W. Lee, K. Yan, H. Yao, H. Wang, W. Li, S. Chu, Y. Cui, *Nat. Nanotechnol.* **2014**, *9*, 618.
- [10] H. Lee, D. J. Lee, Y.-J. Kim, J.-K. Park, H.-T. Kim, *J. Power Sources* **2015**, *284*, 103.
- [11] L. Gireaud, S. Grugeon, S. Laruelle, B. Yrieix, J. M. Tarascon, *Electrochem. Commun.* **2006**, *8*, 1639.
- [12] P. Barai, K. Higa, V. Srinivasan, *J. Electrochem. Soc.* **2018**, *165*, A2654.
- [13] J. Kasemchainan, S. Zekoll, D. Spencer Jolly, Z. Ning, G. O. Hartley, J. Marrow, P. G. Bruce, *Nat. Mater.* **2019**, *18*, 1105.
- [14] X. Zhang, Q. J. Wang, K. L. Harrison, K. Jungjohann, B. L. Boyce, S. A. Roberts, P. M. Attia, S. J. Harris, *J. Electrochem. Soc.* **2019**, *166*, A3639.
- [15] F. Zheng, M. Kotobuki, S. Song, M. O. Lai, L. Lu, *J. Power Sources* **2018**, *389*, 198.
- [16] Y. Yamada, A. Yamada, *J. Electrochem. Soc.* **2015**, *162*, A2406.
- [17] R. Younesi, G. M. Veith, P. Johansson, K. Edström, T. Vegge, *Energy Environ. Sci.* **2015**, *8*, 1905.
- [18] L. Suo, Y. S. Hu, H. Li, M. Armand, L. Chen, *Nat. Commun.* **2013**, *4*, 1481.
- [19] Q. Ma, X. Zhang, A. Wang, Y. Xia, X. Liu, J. Luo, *Adv. Funct. Mater.* **2020**, *30*, 2002824.
- [20] L. Cheng, L. A. Curtiss, K. R. Zavadil, A. A. Gewirth, Y. Shao, K. G. Gallagher, *ACS Energy Lett.* **2016**, *1*, 503.
- [21] J. Wang, Y. Yamada, K. Sodeyama, C. H. Chiang, Y. Tateyama, A. Yamada, *Nat. Commun.* **2016**, *7*, 12032.
- [22] Z. Hu, G. Li, A. Wang, J. Luo, X. Liu, *Batteries Supercaps* **2020**, *3*, 331.
- [23] M. Shin, H. L. Wu, B. Narayanan, K. A. See, R. S. Assary, L. Zhu, R. T. Haasch, S. Zhang, Z. Zhang, L. A. Curtiss, A. A. Gewirth, *ACS Appl. Mater. Interfaces* **2017**, *9*, 39357.
- [24] M. Cuisinier, P. E. Cabelguen, B. D. Adams, A. Garsuch, M. Balasubramanian, L. F. Nazar, *Energy Environ. Sci.* **2014**, *7*, 2697.
- [25] M. A. Philip, P. T. Sullivan, R. Zhang, G. A. Wooley, S. A. Kohn, A. A. Gewirth, *ACS Appl. Mater. Interfaces* **2019**, *11*, 2014.
- [26] M. Shin, A. A. Gewirth, *Adv. Energy Mater.* **2019**, *9*, 1900938.
- [27] X. Ren, L. Zou, S. Jiao, D. Mei, M. H. Engelhard, Q. Li, H. Lee, C. Niu, B. D. Adams, C. Wang, J. Liu, J.-G. Zhang, W. Xu, *ACS Energy Lett.* **2019**, *4*, 896.
- [28] X. Ren, S. Chen, H. Lee, D. Mei, M. H. Engelhard, S. D. Burton, W. Zhao, J. Zheng, Q. Li, M. S. Ding, M. Schroeder, J. Alvarado, K. Xu, Y. S. Meng, J. Liu, J.-G. Zhang, W. Xu, *Chem* **2018**, *4*, 1877.
- [29] S. Wei, Z. Li, K. Kimura, S. Inoue, L. Pandini, D. Di Lecce, Y. Tominaga, J. Hassoun, *Electrochim. Acta* **2019**, *306*, 85.
- [30] X. Fan, L. Chen, X. Ji, T. Deng, S. Hou, J. Chen, J. Zheng, F. Wang, J. Jiang, K. Xu, C. Wang, *Chem* **2018**, *4*, 174.
- [31] K. Shigenobu, A. Nakanishi, K. Ueno, K. Dokko, M. Watanabe, *RSC Adv.* **2019**, *9*, 22668.
- [32] J. Zheng, J. A. Lochala, A. Kwok, Z. D. Deng, J. Xiao, *Adv. Sci.* **2017**, *4*, 1700032.
- [33] D. W. McOwen, D. M. Seo, O. Borodin, J. Vatamanu, P. D. Boyle, W. A. Henderson, *Energy Environ. Sci.* **2014**, *7*, 416.
- [34] M. Dahbi, D. Violeau, F. Ghamouss, J. Jacquemin, F. Tran-Van, D. Lemordant, M. Anouti, *Ind. Eng. Chem. Res.* **2012**, *51*, 5240.
- [35] A. Mauger, C. M. Julien, A. Paoletta, M. Armand, K. Zaghib, *Mater. Sci. Eng., R* **2018**, *134*, 1.
- [36] M. Kerner, N. Plylahan, J. Scheers, P. Johansson, *RSC Adv.* **2016**, *6*, 23327.
- [37] L. Wang, Z. Luo, H. Xu, N. Piao, Z. Chen, G. Tian, X. He, *RSC Adv.* **2019**, *9*, 41837.
- [38] P. Geysens, V. S. Rangasamy, S. Thayumanasundaram, K. Robeyns, L. Van Meervelt, J. P. Locquet, J. Fransaer, K. Binnemans, *J. Phys. Chem. B* **2018**, *122*, 275.
- [39] V. Nilsson, A. Kotronia, M. Lacey, K. Edström, P. Johansson, *ACS Appl. Energy Mater.* **2019**, *3*, 200.
- [40] K. Kwon, J. W. Evans, *Electrochem. Solid-State Lett.* **2002**, *5*, A59.
- [41] M. Z. Kufian, S. R. Majid, *Ionics* **2009**, *16*, 409.
- [42] P. Porion, Y. R. Dougassa, C. Tessier, L. El Ouatani, J. Jacquemin, M. Anouti, *Electrochim. Acta* **2013**, *114*, 95.
- [43] F. Wohde, M. Balabajew, B. Roling, *J. Electrochem. Soc.* **2016**, *163*, A714.
- [44] H. K. Kashyap, H. V. R. Annapureddy, F. O. Rainieri, C. J. Margulis, *J. Phys. Chem. B* **2011**, *115*, 13212.
- [45] W. L. Yuan, X. Yang, L. He, Y. Xue, S. Qin, G. H. Tao, *Front. Chem.* **2018**, *6*, 59.
- [46] T. Weigel, F. Schipper, E. M. Erickson, F. A. Susai, B. Markovsky, D. Aurbach, *ACS Energy Lett.* **2019**, *4*, 508.
- [47] K. Märker, P. J. Reeves, C. Xu, K. J. Griffith, C. P. Grey, *Chem. Mater.* **2019**, *31*, 2545.
- [48] X. Li, L. Jin, D. Song, H. Zhang, X. Shi, Z. Wang, L. Zhang, L. Zhu, *J. Energy Chem.* **2020**, *40*, 39.
- [49] Y. Jin, B. Zhu, Z. Lu, N. Liu, J. Zhu, *Adv. Energy Mater.* **2017**, *7*, 1700715.
- [50] J. Kasnatscheew, M. Evertz, B. Streipert, R. Wagner, R. Kloßsch, B. Vortmann, H. Hahn, S. Nowak, M. Amereller, A. C. Gentsch, P. Lamp, M. Winter, *Phys. Chem. Chem. Phys.* **2016**, *18*, 3956.
- [51] P. Murmann, R. Schmitz, S. Nowak, N. Ignatiev, P. Sartori, I. Čekić-Lasković, M. Winter, *J. Electrochem. Soc.* **2015**, *162*, A1738.
- [52] Y. Zhang, Y. Katayama, R. Tatara, L. Giordano, Y. Yu, D. Fraggedakis, J. G. Sun, F. Maglia, R. Jung, M. Z. Bazant, Y. Shao-Horn, *Energy Environ. Sci.* **2020**, *13*, 183.
- [53] C. H. Chen, J. Liu, K. Amine, *J. Power Sources* **2001**, *96*, 321.
- [54] K. W. Knehr, T. Hodson, C. Bommier, G. Davies, A. Kim, D. A. Steingart, *Joule* **2018**, *2*, 1146.
- [55] G. Salitra, E. Markevich, M. Afri, Y. Talyosef, P. Hartmann, J. Kulisch, Y. K. Sun, D. Aurbach, *ACS Appl. Mater. Interfaces* **2018**, *10*, 19773.
- [56] D. Mukoyama, T. Momma, H. Nara, T. Osaka, *Chem. Lett.* **2012**, *41*, 444.
- [57] T. Osaka, T. Momma, D. Mukoyama, H. Nara, *J. Power Sources* **2012**, *205*, 483.
- [58] T. Osaka, S. Nakade, M. Rajamäki, T. Momma, *J. Power Sources* **2003**, *119*–121, 929.
- [59] T. Momma, M. Matsunaga, D. Mukoyama, T. Osaka, *J. Power Sources* **2012**, *216*, 304.
- [60] J. Qian, W. A. Henderson, W. Xu, P. Bhattacharya, M. Engelhard, O. Borodin, J. G. Zhang, *Nat. Commun.* **2015**, *6*, 6362.
- [61] F. Wu, Q. Li, L. Chen, Q. Zhang, Z. Wang, Y. Lu, L. Bao, S. Chen, Y. Su, *ACS Appl. Mater. Interfaces* **2019**, *11*, 36751.
- [62] J. Zhang, L. Zhou, H. Ming, Y. Wu, W. Wahyudi, Z. Cao, L. Cavallo, L. Wang, J. Ming, *Chem. Commun.* **2019**, *55*, 5713.
- [63] J. Wang, J. Polleux, J. Lim, B. Dunn, *J. Phys. Chem. C* **2007**, *111*, 14925.
- [64] X.-B. Cheng, C. Yan, X. Chen, C. Guan, J.-Q. Huang, H.-J. Peng, R. Zhang, S.-T. Yang, Q. Zhang, *Chem* **2017**, *2*, 258.
- [65] C. Yan, X. B. Cheng, Y. Tian, X. Chen, X. Q. Zhang, W. J. Li, J. Q. Huang, Q. Zhang, *Adv. Mater.* **2018**, *30*, 1707629.
- [66] T. T. Hagos, B. Thirumalraj, C. J. Huang, L. H. Abrha, T. M. Hagos, G. B. Berhe, H. K. Bezabih, J. Cherng, S. F. Chiu, W. N. Su, B. J. Hwang, *ACS Appl. Mater. Interfaces* **2019**, *11*, 9955.
- [67] H. Liu, H. Zhou, B. S. Lee, X. Xing, M. Gonzalez, P. Liu, *ACS Appl. Mater. Interfaces* **2017**, *9*, 30635.
- [68] X. Li, S. Guo, H. Deng, K. Jiang, Y. Qiao, M. Ishida, H. Zhou, *J. Mater. Chem. A* **2018**, *6*, 15517.
- [69] X. Cao, X. Ren, L. Zou, M. H. Engelhard, W. Huang, H. Wang, B. E. Matthews, H. Lee, C. Niu, B. W. Arey, Y. Cui, C. Wang, J. Xiao, J. Liu, W. Xu, J.-G. Zhang, *Nat. Energy* **2019**, *4*, 796.
- [70] E. Peled, S. Menkin, *J. Electrochem. Soc.* **2017**, *164*, A1703.
- [71] D. Aurbach, E. Zinigrad, Y. Cohen, H. Teller, *Solid State Ionics* **2002**, *148*, 405.
- [72] J. Zheng, M. H. Engelhard, D. Mei, S. Jiao, B. J. Polzin, J.-G. Zhang, W. Xu, *Nat. Energy* **2017**, *2*, 17012.
- [73] B. S. Parimalam, B. L. Lucht, *J. Electrochem. Soc.* **2018**, *165*, A251.
- [74] A. M. Andersson, M. Herstedt, A. G. Bishop, K. Edström, *Electrochim. Acta* **2002**, *47*, 1885.
- [75] C.-C. Su, M. He, R. Amine, Z. Chen, R. Sahore, N. Dietz Rago, K. Amine, *Energy Storage Mater.* **2019**, *17*, 284.
- [76] A. Wang, S. Kadam, H. Li, S. Shi, Y. Qi, *npj Comput. Mater.* **2018**, *4*, 1.
- [77] A. Eftekhari, *Sustainable Energy Fuels* **2017**, *1*, 2053.
- [78] B. D. Adams, J. Zheng, X. Ren, W. Xu, J.-G. Zhang, *Adv. Energy Mater.* **2018**, *8*, 1702097.
- [79] S. Randau, D. A. Weber, O. Kötz, R. Koerver, P. Braun, A. Weber, E. Ivers-Tiffée, T. Adermann, J. Kulisch, W. G. Zeier, F. H. Richter, J. Janek, *Nat. Energy* **2020**, *5*, 259.

Manuscript received: August 14, 2020

Revised manuscript received: September 14, 2020

Accepted manuscript online: September 22, 2020

Version of record online: October 29, 2020